Yang, R., et al., 2021, Enhanced Quaternary exhumation in the Namche Barwa syntaxis, eastern Himalaya: Geology, v. 49, https://doi.org/10.1130/G48595.1

Supplemental Material

Enhanced Quaternary exhumation in the Namche Barwa syntaxis, eastern Himalaya

Rong Yang[1], Frédéric Herman[2], Ting Liu[1], Rabiul Haque Biswas[2], Maria Giuditta Fellin[3], Yuntao Tian[4], Junfeng Gong[1], Ruohong Jiao[5], Colin Maden[3], Hanlin Chen[1]

This file includes:

Supplementary Methods:

parameters presented in Table S5.

Figure S4. Plots of exhumation rates, resolution and predicted against measured ages using parameters presented in Table S5.

Figure S5. Plots of exhumation rates, resolution and predicted against measured ages using parameters presented in Table S5.

Figure S6. Plots of exhumation rates, resolution and predicted against measured ages using parameters presented in Table S5.

Figure S7. Plots of exhumation rates, resolution and predicted against measured ages using parameters presented in Table S5.

Figure S8. Representative TL growth curve of one signal at 310-320°C for sample YG1701. The gray points are the experimental data. A correction for athermal loss had been made. The un-faded regenerative dose responses (black points) are fitted and the natural TL (nobs), green point, is derived from interpolation onto the fading-corrected dose response curve.

Figure S9. Distribution of kinetic parameters along the glow curve temperature of 200 to 420°C for sample YG1701. A) trap depth (E), B) thermal frequency factor (s) and C) kinetic order of detrapping.

Figure S10. Representative athermal fading of one signal at 310-320° and fitting for sample YG1701.

SUPPLEMENTARY METHODS

1. Sampling locations

14 bedrock samples over a distance of ~ 200 km along the Yigong River course were collected during two field campaigns in 2016 and 2018. The elevation of these samples ranges from 2063 m to 3977 m. We also collected six modern sand samples from the Yigong drainage basin. The locations of these samples are shown in Fig.1 and also in Table S1.

2. Zircon U-Pb dating

Zircon U-Pb analyses were carried out at the LA-ICPMS laboratory of Zhejiang University.

The laser system used was an Analyte HE (Teledyne CETAC technologies, USA) coupled with a HelEx II two-volume sample chamber. The ICPMS used was an iCAP RQ (Thermofisher, USA). The ablation crater diameters were 35 μm throughout this study. Zircon 91500 were measured twice before and after 6 spot analyses of samples. The results of the sample analyses were processed with the ICPMSDataCal software. The signal intensities (counts per ppm) for each element were calibrated against the Zircon 91500 and NIST SRM 612. The Plešovice zircon (every 6 spot analyses) was measured as unknown. Calculation of mean ages and plotting of concordia diagrams for all U–Pb data in this study was done with the Isoplot/Ex v.4 program (Table S2 and Figure S1).

3. Zircon (U-Th)/He sample preparation and analytical techniques

For zircon (U-Th)/He dating, zircons with tetragonal prism width of at least 60 μm were selected. Each grain was then photographed to measure its length and width and the heights of its pyramidal terminations for the FT factor calculation. Fission Canyon Tuff zircons were used as external standards and analyzed together with the samples. ^{4}He abundances for each grain were determined by degassing with a diode laser at 1075 °C for 45 minutes and measuring the released gas on a magnet sector field mass spectrometer equipped with a Baur-Signer ion source at ETH Zürich. Multiple re-extractions were performed at progressively higher temperatures until the re-extracted gas was ≤3% of the total. To measure the parent nuclide contents of the degassed zircons, grains were dissolved in concentrated HF and spiked with an isotopically distinct U-Th solution. U and Th concentrations were measured on an inductively coupled plasma mass spectrometer at ETH Zürich (ElementXR). Ages were corrected for the α-ejection factor following Ketcham et al. (2011) and reported in Table S3.

4. Apatite (U-Th)/He sample preparation and analytical techniques

For apatite (U-Th)/He dating, apatite grains with euhedral morphology and no visible inclusions were selected under a polarized microscope. The dimensions of each grain were measured and only grains > 60 μm in both length and width were considered to be suitable for (U-Th)/He dating. For each sample, at least three grains were selected. Durango apatites were used as external standards and analyzed together with the samples. ^{4}He abundances for each grain were determined by degassing at a fixed temperature heated by a diode laser (in the range of 800-900°C) for three minutes and measuring the released gas on a magnet sector field mass spectrometer equipped with a Baur-Signer ion source at ETH Zurich. After degassing, each crystal was weighed before and after adding the U-Th-Sm isotope spike. The same grain was then dissolved in HNO_3. The U-Th-Sm concentration of each dissolved grain was then measured on an inductively coupled plasma quadrupole mass spectrometer at ETH Zürich (PerkinElmer ElanDRC-e). The age calculation was processed by applying the α-ejection correction factor, FT, following Ketcham et al. (2011) to each crystal to derive a corrected (U-Th)/He age (Table S4). The age error was derived from the analytical uncertainties in U, Th, and Sm measurements, and the variance of the single grain ages.

5. Inversion of exhumation rates from thermochronometric ages

To invert exhumation rates from thermochronometric ages, we used an inversion approach of Fox et al. (2014). This approach converts thermochronometric age to exhumation rate based on the fact that the depth to the closure isotherm is the integral of erosion rates from the cooling age to the present. The time dimension is discretized over a finite number of time intervals and erosion rate is determined for each of these intervals. The heat transfer equation with both heat

conduction and advection is solved with a one-dimensional thermal model, accounting for the effects of topography on the shape of the isotherms. The kinetic parameters for helium diffusion in apatite and zircon are from Farley (2000) and Reiners et al. (2004), respectively, for fission track annealing in apatite and zircon from Ketcham et al. (1999) and Brandon et al. (1998), respectively, and for argon diffusion in biotite from Grove and Harrison (1996). To initialize the inversion, an *a priori* erosion rate and its variance are used and the *a priori* is iteratively updated to a posterior erosion rate that maximizes the fit to the data using the non-linear least squares method. In this approach, thermochronometric data are spatially correlated by imposing a spatial correlation length which ensures that erosion rates vary smoothly in space.

As most of the thermochronometric ages in the syntaxis and its close vicinities are < 10 Ma and the resolution of inversion depends on the number of ages within the time range over which exhumation is inverted, we ran the inversion for a 10 million year exhumation history. Since exhumation history obtained from the inversion may depend on the choice of the *a priori* erosion rate and its variance, the initial geothermal gradient, the spatial correlation length, and the time intervals, we used different values of these parameters to test the sensitivity of the results (Table S5). For each inversion, we report the inverted exhumation rates together with the resolution and the predicted ages from the inversion (Figures S2-S7). Before 6 Ma, exhumation rates in most of the syntaxis region, especially in the core of the syntaxis, are not well resolved due to the paucity of ages older than 6 Ma. Therefore, we only report the results in the last 6 Ma for all the inversions except for inversion with a time interval of 4 Ma in which exhumation rates in the last 8 Ma are reported. Among all the models (Figures S2-S7), it appears that inversion with *a priori* erosion rate of 2 km/Ma and a variance of 1 km/Ma, an initial

geothermal gradient of ~30 °C/km, a spatial correlation length of 10 km, and a time interval of 2 Ma best predicts the thermochronometric ages(Figure S2). A larger spatial correlation length of 20 km tends to increase the resolution of the results but also leads to more scatters between the observed and predicted data (Figure S5). Simulation with a lower *a priori* erosion rate of 0.5 ±0.3 km/Ma (Figure S7), a shorter time interval of 1 Ma (Figure S3) and a lower initial geothermal gradient of ~20 °C/km (Figure S6), respectively, yields relatively worse fit to the observed ages. A larger time interval of 4 Ma (Figure S4) also predicts the ages well except relatively more scatters between the observed and predicted data, in particular, for ages older that ~ 5 Ma compared to a time interval of 2 Ma. Thus we used results presented in Figure S2 in the main text for interpretation and discussion.

6. Thermoluminescence (TL) analysis of K-feldspar

Thermoluminescence of K-feldspar is a newly developed multi-thermochronometer based on the fact that thermoluminescence signals from feldspar arise from continuous distribution of trapping energies having ranges of thermal stabilities (Biswas et al., 2018; Duller, 1997; Pagonis et al., 2014) and that the time-dependent accumulation of TL signals is a function of radiation-induced TL growth and TL decay via thermal and athermal pathways. For a given trap depth, natural thermoluminescence(TL) in rocks can be described by a dynamic equilibrium level where radiation-induced TL growth is balanced by TL decay via thermal and athermal pathways. This process can be expressed by the following equation as described by Biswas et al. (2018) and Guralnik et al. (2015):

$$\frac{d}{dt}\left(\bar{n}(r',t)\right) = \frac{\dot{D}}{D_0}(1-\bar{n}(r',t))^a - se^{-\frac{E}{kT}}\left(\bar{n}(r',t)\right)^b - \tilde{s}e^{-\rho'^{-\frac{1}{3}}r'}\bar{n}(r',t)$$

where $\bar{n}$ is equal to n/N (n is the number of trapped electrons at time t and temperature T, and

N is the total number of available traps), $\dot{D}$ is the dose rate due to ambient radioactivity, D_0 is the onset of dose saturation, a and b are the kinetic orders of trapping and thermal detrapping, respectively, E is the thermal trap depth or activation energy, s and $\tilde{s}$ are the thermal and athermal frequency factors respectively. ρ' is dimensionless recombination center density, which is the measure of distance (r') dependent athermal fading. After constraining these seven kinetic parameters ($\dot{D}$, D_0, a, s, E, b, ρ') associated with TL growth, thermal and athermal decays, the observed TL signals can be inverted for reconstruction of an exhumation history.

These kinetic parameters were constrained through lab experiments at the University of Lausanne. Rock sample was processed under subdued red light. To measure the dose rate ($\dot{D}$) due to ambient radioactivity, a portion of rock sample was sent to ActLabs, Canada, to measure U, Th, and K concentrations using inductively coupled plasma mass spectrometry. Dose rate ($\dot{D}$) was then estimated following DRAC (Durcan et al. 2015) (Table S6).

To measure the thermoluminescence signals and to constrain the kinematic parameters associated with TL growth, thermal and athermal decays, the outer part of the rock sample (at least 1 cm from the surface) was cut using diamond saw with constant water flow to avoid frictional heating while extraction and only the interior part was extracted. Sample was then gently hand crushed and sieved to separate the 150-250 μm grain size fraction. To extract K-feldspar from this size fraction, 10% HCl and 30% H_2O_2 were first used to remove carbonate and organic matter attached to the grains and then the magnetic fractions were removed by a hand magnet once the grains were dried. After that, the K-feldspar grains were separated using sodium polytungstate with a density of <2.58 gm/cm3.

The obtained K-feldspar grains were mounted on stainless steel discs and TL signals were measured by the Risø TL/OSL reader equipped with a 90Sr/90Y irradiation source (~0.25 Gy/s) at the University of Lausanne. Measurements of TL were processed with three experiments. In the first experiment, the TL growth curves were reconstructed. In the second experiment, the thermal decay of TL signals was measured and in the third experiment, the athermal decay of TL signals was measured. Three aliquots were measured for the sample.

The growth of TL due to ambient radioactivity in nature was reproduced in the laboratory at temperatures between 0–450 °C using the following single aliquot regeneration (SAR) protocol: natural + TL + test dose (25 Gy) +TL + regenerative doses +TL + test dose (25 Gy) +TL, where the regenerative dose varies as 0, 25, 50, 125, 250, 500, 1000, 2000, and 4000 Gy. In this SAR protocol, the dose response curve was constructed by normalizing the regenerative TL signals with fixed test dose TL signals to monitor the sensitivity change that may arise due to repeated cycle of dosing and heating. After correcting for athermal fading during laboratory irradiation time, the un-faded regenerative dose responses was fitted separately for seven signals (250–320 °C, 10 °C interval) as TL signals below 250 °C are too sensitive to temperature over the range where the minerals behave expectedly to obtain the natural TL signals in the mineral ($\bar{n}$) and the kinetic parameters of the onset of dose saturation (D_0) and the kinetic orders of trapping (a) (Table S7, Figure S8).

Thermal decay parameters, activation energy (E), frequency factor (s) and order of kinetics for thermal detrapping (b) of seven TL signals (250–320 °C, 10 °C interval) were estimated using fitting of sub-glow peaks, obtained through Tm-Tstop method by partially heating the dosed sample to a temperature (Tstop) where Tstop varies from 50 °C to 430 °C at a 5 °C

interval. After that, sample was cooled down to room temperature and then reheated to a high temperature (450 °C) to record all of the remaining glow curve from which the temperature (Tm) corresponding to the peak TL intensity was extracted. The sub-peaks, subtraction of two consecutive fractional glow curves, are fitted with the general order kinetics TL equation (Kitis et al., 1998) and the distributions of thermal kinetic parameters were obtained and kinetic parameters of the region of interest (250–320 °C, 10 °C interval) were extracted from the distributions (Table S7, Figure S9).

Athermal loss of TL signals was measured for the same three aliquots for different delay times ranging from instantaneous measurement to 3 days after an arbitrary irradiation of 75 Gy and cut-heat of 200 °C. A test dose, which is equal to the regeneration dose, was used for normalization and the kinetic parameters (ρ') for athermal decay was determined from the relationship between the TL signals and the delay times (Table S7, Figure S10). The athermal frequency factor could be different to the thermal frequency factor and equal to 3×10^{15} s^{-1} (Huntley, 2006).

To invert an exhumation history from TL signals, 30,000 of t–Z paths (time-depth path) were generated using a Monte Carlo approach with monotonically decreasing depth over a time period of 1 Ma. This time period is long enough to have the exhumation history to be recorded by the TL signals. Each t-Z path was first converted to a cooling path (time-temperature path) by solving the 1-D heat transfer equation

$$\frac{\partial T}{\partial t} = k\frac{d^2T}{dZ^2} + \dot{e}(t)\frac{dT}{dt}$$

where k is the thermal diffusivity and $\dot{e}$ is the exhumation rate, which is time dependent. TL signals ($\bar{n}$) were then predicted by using the kinetic parameters constrained in the previous

sections. The predicted TL signals were compared with the observed TL signals and the best t-Z paths were determined by calculating the misfit between the observed and predicted TL signals. A probability distribution was constructed by summing the number of accepted t–Z paths that passed through each grid cell after dividing the time (2–0 Ma) and depth (25–0 km) axes into 2000 × 2000 grids. To quantify the cooling rate, 68% (1σ) and 95% (2σ) confidence intervals of the distribution and the by taking the time derivative of the median and confidence interval lines of the probability density plots.

To invert exhumation history, seven TL signals (250–320 °C, 10 °C interval) of sample YG1701 were used since TL signals below 250 °C are too sensitive to temperature. We used a thermal diffusivity of 30 km2/Ma, a crustal depth of 25 km, and a reasonable initially unperturbed geothermal gradient of 30°C/km. The inversion was performed over a time period of 1 Ma before present and 30,000 randomly generated thermal paths were used to establish the exhumation history. The best-fit model is chosen based on the agreement between the observed and predicted TL signals.

7. ^{10}Be analysis

Quarts were separated from sand samples following standard procedures of magnetic and heavy-liquid separation and acid dissolutions. The size fraction of 250-1000 μm were used for ^{10}Be measurement at the AMS center of Institute of Earth and Environment, Chinese Academy of Sciences. Erosion rates were calculated using the online program of CRONUS (Balco et al., 2008) based on the time-dependent form of the Lal (1991)/Stone (2000) scaling model and are reported in Table S8.

Reference

Balco, G., Stone, J.O., Lifton, N.A., and Dunai, T.J., 2008, A complete and easily accessible means of calculating surface exposure ages or erosion rates from ^{10}Be and ^{26}Al measurements: Quat. Geochronol., v. 3, p. 174–195.

Biswas, R. H., Herman, F., King, G. E., and Braun, J., 2018, Thermoluminescence of feldspar as a multi-thermochronometer to constrain the temporal variation of rock exhumation in the recent past: Earth and Planetary Science Letters, v. 495, p. 56-68.

Brandon, M.T., Roden-Tice, M.K., and Garver, J.I., 1998, Late Cenozoic exhumation of the Cascadia accretionary wedge in the Olympic Mountains, Northwest Washington State: Geol. Soc. Am. Bull., v.110, p. 985–1009.

Duller, G.A.T., 1997, Behavioral studies of stimulated luminescence from feldspars: Radiation Measurements, v. 27, p. 663-694.

Durcan, J.A., King, G.E., and Duller, G.A.T., 2015, DRAC: Dose Rate and Age Calculator for trapped charge dating: Quat. Geochronol, v. 28, p. 54-61.

Farley, K., 2000, Helium diffusion from apatite: general behavior as illustrated by Durango fluorapatite: J. Geophys. Res., Solid Earth (1978–2012), v. 105, p. 2903–2914.

Fox, M., Herman, F., Willett, S., and May, D., 2014, A linear inversion method to infer exhumation rates in space and time from thermochronometric data: Earth Surf. Dyn., v. 2, p. 47–65.

Grove, M. and Harrison, T.M., 1996, $^{40}Ar^{*}$ diffusion in Fe-rich biotite, Am. Mineral., v. 81, p. 940–51.

Guralnik, B., Jain, M., Herman, F., Paris, R.B., Harrison, T.M., Murray, A.S., Valla, P.G., and Rhodes, E.J., 2013, Effective closure temperature in leaky and/or saturating

thermochronometers: Earth and Planetary Science Letters, v. 384, p. 209-218.

Huntley, D.J., 2006, An explanation of the power-law decay of luminescence: Journal of Physics: Condensed Matter, v. 18, p. 1359-1365.

Ketcham, R.A., Donelick, R.A., and Carlson, W.D., 1999, Variability of apatite fission-track annealing kinetics: III. Extrapolation to geological time scales: Am. Mineral., v. 84, p. 1235–1255.

Ketcham, R. A., Gautheron, C., and Tassan-Got, L., 2011, Accounting for long alpha-particle stopping distances in (U–Th–Sm)/He geochronology: refinement of the baseline case: Geochimica et Cosmochimica Acta, v. 75, p. 7779-7791.

King, G. E., Herman, F., and Guralnik, B., 2016, Northward migration of the eastern Himalayan syntaxis revealed by OSL thermochronometry: SCIENCE v. 353, p. 800-804.

Kitis, G., Gomez-Ros, J.M., and Tuyn, J.W.N., 1998, Thermoluminescence glow-curve deconvolution functions for first, second and general orders of kinetics: Journal of Physics D: Applied Physics, v. 31, p. 2636-2641.

Lal, D., 1991, Cosmic ray labeling of erosion surfaces: in situ nuclide production rates and erosion models: Earth and Planetary Science Letters, v. 104, p. 424–439.

Pagonis, V., Morthekai, P., and Kitis, G., 2014, Kinetic analysis of thermoluminescence glow curves in feldspar: evidence for a continuous distribution of energies: Geochronometria, v. 41, p. 168-177.

Reiners, P.W., Spell, T.L., Nicolescu, S., and Zanetti, K.A., 2004, Zircon (U–Th)/He thermochronometry: He diffusion and comparisons with 40Ar/39Ar dating: Geochim. Cosmochim. Acta, p. 68, v. 1857–1887.

Stone, J.O., 2000, Air pressure and cosmogenic isotope production: J. Geophys. Res., v. 105, p. 23753–23759.

Table S1. Sample information

Sample	Longitude (°E)	Latitude (°N)	Elevation (m)	Lithology
YG1701	95.066	30.098	2063	Gneiss
YG1702	95.063	30.116	2063	Granitoids
YG1802	94.953	30.164	2184	Gneiss
YG1805	94.791	30.335	2352	Granitoids
YG1807	94.747	30.286	2279	Granitoids
YG1810	94.733	30.293	2477	Granitoids
YG1811	94.705	30.3	2442	Granitoids
YG1812	94.626	30.306	2548	Granitoids
YG1814	94.521	30.324	2655	Granitoids
YG1815	94.44	30.349	2742	Granitoids
YG1818	94.157	30.441	2928	Granitoids
YG1820	94.053	30.483	3108	Granitoids
YG1821	93.81	30.591	3702	Granitoids
YG1822	93.634	30.588	3977	Granitoids
YG1801	95.066	30.099	2021	Modern sands
YG1803	94.923	30.178	2265	Modern sands
YG1813	94.623	30.309	2523	Modern sands
YG1816	94.43	30.357	2775	Modern sands
YG1819	94.061	30.481	3101	Modern sands
YG1823	93.228	30.638	4488	Modern sands

Table S2. LA- ICPMS zircon U–Pb data for samples from the Yigong River.

Sample	U (ppm)	Th (ppm)	$^{232}Th/^{238}U$	$^{207}Pbr/^{206}Pbr$	1σ error	$^{207}Pbr/^{235}U$	1σ error	$^{206}Pbr/^{238}U$	1σ error	$^{206}Pb/^{238}U$ (Ma)	1σ error (Ma)
YG1701-1	652.76	359.45	0.55	0.0473	0.0015	0.0985	0.0036	0.015	0.0003	96	2
YG1701-2	363.72	279.91	0.77	0.0494	0.0017	0.1304	0.0046	0.0194	0.0004	124	2
YG1701-3	326.89	217.24	0.66	0.0502	0.0015	0.1482	0.0045	0.0214	0.0003	137	2
YG1701-4	406.37	331.98	0.82	0.0504	0.0017	0.1303	0.0049	0.0188	0.0003	120	2
YG1701-5	636.86	296.9	0.47	0.0487	0.0014	0.1235	0.0038	0.0184	0.0003	118	2
YG1701-6	525.35	470.23	0.9	0.0506	0.0018	0.1513	0.0049	0.0218	0.0003	139	2
YG1701-7	511.55	365.65	0.71	0.0466	0.0015	0.1007	0.0036	0.0154	0.0003	98	2
YG1701-8	456.95	394.71	0.86	0.0484	0.0013	0.1261	0.0034	0.0191	0.0003	122	2
YG1701-9	655.58	180.44	0.28	0.049	0.0021	0.0558	0.0022	0.0082	0.0001	52.9	0.8
YG1701-10	1370.27	487.13	0.36	0.0496	0.0012	0.1004	0.0026	0.0148	0.0003	95	2
YG1701-11	362.63	258.19	0.71	0.0495	0.0018	0.1296	0.0046	0.0192	0.0003	123	2
YG1701-12	1315.31	110.2	0.08	0.0477	0.0014	0.0407	0.0013	0.0062	0.0001	39.8	0.6
YG1701-13	2143.03	234.6	0.11	0.0494	0.0008	0.1221	0.0022	0.018	0.0002	115	1
YG1701-14	1357.47	388.48	0.29	0.049	0.001	0.124	0.0026	0.0184	0.0002	118	2
YG1701-15	727.86	304.88	0.42	0.0499	0.0013	0.0954	0.0033	0.0139	0.0003	89	2
YG1701-16	436.24	250.81	0.57	0.0495	0.0017	0.1158	0.0042	0.017	0.0003	109	2
YG1701-17	1189.8	420.4	0.35	0.0487	0.0016	0.032	0.0011	0.0048	0.0001	30.8	0.4
YG1701-19	1172.29	468.96	0.4	0.0516	0.002	0.1416	0.0065	0.0203	0.0007	129	5
YG1701-20	1086.5	418.46	0.39	0.0501	0.001	0.1409	0.0031	0.0205	0.0003	131	2
YG1701-21	1385.9	164.09	0.12	0.0491	0.0009	0.1096	0.0022	0.0162	0.0002	104	1
YG1701-22	516.15	269.27	0.52	0.0504	0.0012	0.1343	0.003	0.0196	0.0002	125	1
YG1701-23	777.07	276.18	0.36	0.0482	0.001	0.0995	0.0025	0.0151	0.0003	97	2

YG1701-25	450.15	329.58	0.73	0.0503	0.0018	0.1122	0.004	0.0162	0.0002	104	1
YG1701-26	211.2	132.96	0.63	0.049	0.0018	0.1262	0.0046	0.0187	0.0002	120	2
YG1701-27	1103.15	209.46	0.19	0.0475	0.001	0.0556	0.0015	0.0085	0.0002	55	1
YG1701-28	838.43	1252.12	1.49	0.0508	0.0011	0.1409	0.0029	0.0202	0.0002	129	1
YG1701-29	363.67	232.75	0.64	0.0507	0.0015	0.117	0.0034	0.0169	0.0002	108	1
YG1701-30	636.93	284.97	0.45	0.0497	0.001	0.1452	0.0032	0.0212	0.0003	135	2
YG1701-31	519.44	257.03	0.49	0.0505	0.0017	0.1111	0.0037	0.0161	0.0003	103	2
YG1701-32	745.3	325.05	0.44	0.0487	0.0015	0.0749	0.0021	0.0113	0.0002	73	1
YG1701-33	1029.26	328.93	0.32	0.05	0.0011	0.1386	0.003	0.0202	0.0002	129	1
YG1701-34	1168.85	149.17	0.13	0.0477	0.0013	0.0469	0.0013	0.0072	0.0001	46	0.5
YG1701-35	1622.31	1213.84	0.75	0.0487	0.0011	0.126	0.0026	0.0188	0.0002	120	1
YG1701-37	220.02	175.34	0.8	0.0488	0.0018	0.1243	0.0043	0.0185	0.0003	118	2
YG1802-1	228.72	216.15	1.14	0.0791	0.0019	2.1087	0.0468	0.1919	0.0028	1174	22
YG1802-2	179.46	313.83	0.61	0.068	0.0016	1.2349	0.0289	0.1298	0.0019	869	26
YG1802-3	177.05	74.1	2.53	0.0568	0.0036	0.7484	0.0383	0.0905	0.002	483	75
YG1802-4	166.74	271.16	0.66	0.0754	0.0016	1.9509	0.0398	0.1855	0.0028	1078	20
YG1802-5	284.97	509.03	0.61	0.072	0.0016	1.571	0.0371	0.1553	0.0025	987	24
YG1802-6	83.03	199.72	0.45	0.1042	0.0023	4.311	0.0924	0.2958	0.0046	1682	60
YG1802-7	279.78	226.57	1.32	0.0742	0.002	1.6754	0.0422	0.1624	0.0025	1048	27
YG1802-8	235.15	157.89	1.64	0.0864	0.0022	2.8264	0.0725	0.2345	0.0036	1348	27
YG1802-9	397.73	477.34	0.89	0.0954	0.0017	3.6384	0.0653	0.273	0.0035	1536	17
YG1802-10	430.85	613.75	0.76	0.0784	0.0015	1.9645	0.0404	0.1799	0.0026	1156	20
YG1802-11	128.72	585.73	0.23	0.0885	0.0016	2.7809	0.0554	0.2257	0.0032	1393	19
YG1802-12	192.14	339.95	0.61	0.0755	0.0017	1.9032	0.0445	0.1831	0.0028	1081	24
YG1802-13	230.95	519.12	0.47	0.0668	0.0015	1.1726	0.0274	0.1268	0.0018	781	77
YG1802-14	171.85	256.23	0.74	0.076	0.0018	1.8654	0.0432	0.1787	0.0026	1095	24

YG1802-15	209.19	848.91	0.27	0.0596	0.0015	0.6727	0.0171	0.0815	0.0013	588	30
YG1802-16	41.22	62.44	0.7	0.0814	0.0032	1.9796	0.0772	0.1764	0.0033	1085	122
YG1802-17	111.04	200.54	0.58	0.0659	0.002	1.0614	0.0354	0.1157	0.0021	721	114
YG1802-18	693.64	1092.53	0.69	0.0584	0.0014	0.6859	0.017	0.0845	0.0013	547	29
YG1802-19	155.54	838.5	0.2	0.076	0.0016	1.8434	0.0393	0.1737	0.0024	1096	22
YG1802-20	437.27	724.08	0.66	0.0777	0.0016	2.0405	0.0411	0.1887	0.0027	1140	20
YG1802-21	236.96	351.59	0.73	0.0769	0.0016	1.8902	0.0405	0.1763	0.0025	1119	22
YG1802-22	150.85	197.69	0.83	0.165	0.003	10.3573	0.1992	0.4506	0.0067	2460	55
YG1802-23	200.48	318.08	0.68	0.0764	0.002	1.7596	0.0458	0.166	0.0027	999	94
YG1802-24	258.17	762.32	0.38	0.0576	0.0016	0.6101	0.0172	0.0759	0.0013	457	96
YG1802-25	213.47	187.57	1.24	0.0595	0.0023	0.6507	0.0235	0.0797	0.0015	587	46
YG1802-26	172.42	449.79	0.41	0.0615	0.0017	0.7444	0.0191	0.0879	0.0015	658	28
YG1802-27	160.82	379.39	0.46	0.0703	0.0018	1.2796	0.0315	0.132	0.0021	942	26
YG1802-28	291.16	245.45	1.27	0.0705	0.0021	1.457	0.0428	0.1478	0.0021	942	37
YG1802-29	437.52	552.87	0.83	0.0985	0.0018	3.6637	0.0695	0.2658	0.0032	1579	61
YG1802-30	83.01	1424.71	0.06	0.0608	0.0013	0.8063	0.0178	0.0948	0.0013	632	26
YG1802-31	408.14	338.85	1.15	0.075	0.0018	1.9504	0.0472	0.1875	0.003	1069	25
YG1802-32	407.81	261.57	1.7	0.0591	0.0019	0.6841	0.0213	0.084	0.0013	570	41
YG1802-33	458.34	307.33	1.64	0.0592	0.002	0.6361	0.02	0.0762	0.0012	574	42
YG1802-34	120.73	260.15	0.5	0.1988	0.0034	13.3872	0.2313	0.4812	0.006	2832	39
YG1805-1	2712.32	1909.53	1.48	0.0493	0.002	0.0782	0.0029	0.0113	0.0002	72.6	1
YG1805-2	1094.97	2854.5	0.43	0.0475	0.0017	0.0763	0.0027	0.0114	0.0002	73	1
YG1805-3	1862.92	5486.22	0.36	0.0491	0.0014	0.083	0.0024	0.0122	0.0002	78	1
YG1805-4	829.31	4708.85	0.19	0.0494	0.0014	0.0792	0.0022	0.0114	0.0002	73	1
YG1805-5	1295.13	1859.01	0.75	0.0482	0.0018	0.0785	0.0028	0.0116	0.0002	74	1
YG1805-6	1462.73	3718.53	0.46	0.0468	0.0017	0.0779	0.0027	0.0118	0.0002	76	2

YG1805-7	3255.86	1801.37	1.98	0.0461	0.0018	0.0722	0.0025	0.0108	0.0002	69	1
YG1805-8	1042.69	647.37	1.72	0.044	0.0042	0.0852	0.0061	0.0123	0.0004	79	3
YG1805-9	453.03	2234.6	0.21	0.0474	0.0016	0.082	0.0027	0.0125	0.0002	80	1
YG1805-10	2686.09	8317.42	0.35	0.0466	0.0012	0.079	0.0022	0.0121	0.0002	77	1
YG1805-11	2380.78	2405.5	0.64	0.0448	0.0018	0.0775	0.0034	0.0117	0.0002	75	1
YG1805-12	985.04	1362.61	0.77	0.0478	0.0027	0.0784	0.0035	0.0114	0.0002	73	1
YG1805-14	1011.12	1776.49	0.61	0.0502	0.0018	0.0852	0.003	0.0122	0.0002	78	1
YG1805-15	646.95	1728.8	0.42	0.0485	0.0025	0.0846	0.0035	0.0126	0.0002	81	1
YG1805-16	1078.61	2232.88	0.55	0.0488	0.0019	0.0854	0.003	0.0126	0.0002	81	1
YG1805-17	1618.95	4681.82	0.4	0.0477	0.0015	0.0813	0.0023	0.0124	0.0002	79	1
YG1805-18	777.11	1562.67	0.58	0.047	0.0021	0.0832	0.003	0.0119	0.0002	76	1
YG1805-19	1077.87	2382.64	0.51	0.0474	0.0017	0.0823	0.0028	0.0122	0.0002	78	1
YG1805-20	191.08	1579.55	0.13	0.0476	0.0024	0.0773	0.0037	0.0114	0.0002	73	2
YG1805-21	633.24	2122.3	0.32	0.0481	0.0019	0.0804	0.003	0.0121	0.0002	78	1
YG1805-22	762.55	1616.59	0.53	0.0451	0.002	0.0832	0.0029	0.0124	0.0002	80	1
YG1805-23	923.77	1226.28	0.84	0.0438	0.0027	0.0806	0.0041	0.0119	0.0003	76	2
YG1805-24	827.64	1353.17	0.64	0.0456	0.002	0.0802	0.0031	0.0122	0.0002	78	1
YG1805-25	1747.31	9760.07	0.19	0.0468	0.0011	0.0892	0.0023	0.0137	0.0002	88	2
YG1805-26	569.4	528.21	1.13	0.0509	0.0068	0.0797	0.0076	0.0113	0.0006	73	4
YG1805-27	1086.03	6049.68	0.19	0.0481	0.0013	0.0829	0.0022	0.0125	0.0002	80	1
YG1805-28	955.79	1667.13	0.63	0.0494	0.002	0.0874	0.003	0.0122	0.0002	78	1
YG1815-1	820.68	1936.51	0.48	0.0469	0.0017	0.0781	0.0028	0.0118	0.0002	76	1
YG1815-2	1249.322	1583	0.92	0.0484	0.0023	0.0792	0.0035	0.0115	0.0002	74	1
YG1815-3	675.76	2285.42	0.34	0.0505	0.0018	0.0803	0.003	0.0114	0.0002	73	1
YG1815-4	511.02	2333.71	0.26	0.0496	0.0023	0.0775	0.0033	0.0112	0.0002	72	1
YG1815-6	2117.68	3152.77	0.75	0.0493	0.0015	0.0834	0.0025	0.0122	0.0002	78	1

YG1815-7	836.85	1624.14	0.62	0.0487	0.0021	0.0789	0.0031	0.0115	0.0002	74	1
YG1815-9	1084.86	2346.52	0.55	0.0511	0.0022	0.0806	0.0031	0.0113	0.0002	73	1
YG1815-10	608.2	914.45	0.78	0.0501	0.0043	0.0778	0.0056	0.0111	0.0003	71	2
YG1815-11	1649.76	4204	0.45	0.0472	0.0015	0.0761	0.0024	0.0113	0.0002	72	1
YG1815-12	1137.47	2810.4	0.48	0.0512	0.0022	0.0862	0.0034	0.0121	0.0002	78	1
YG1815-13	1143.54	1738.87	0.76	0.0483	0.0024	0.0773	0.0035	0.0108	0.0002	69	1
YG1815-15	1134.66	1659.47	0.8	0.0501	0.0027	0.0801	0.0041	0.0113	0.0002	72	2
YG1815-16	1652	1359.71	1.45	0.0491	0.0028	0.0748	0.0042	0.0109	0.0002	70	1
YG1815-17	13138.02	7675.64	2.02	0.0492	0.003	0.0701	0.0046	0.01	0.0002	64	1
YG1815-18	1392.51	9281.85	0.17	0.0496	0.0013	0.087	0.0023	0.0126	0.0002	81	1
YG1815-19	1996.94	2873.26	0.83	0.0506	0.0022	0.0765	0.0033	0.0109	0.0003	70	2
YG1815-20	2102.18	1785.51	1.41	0.0497	0.0022	0.0754	0.0031	0.0109	0.0002	70	1
YG1815-21	1377.26	1541.76	1.06	0.051	0.0049	0.0888	0.0076	0.0118	0.0004	75	2
YG1815-22	634.44	3059.55	0.23	0.0471	0.0015	0.079	0.0024	0.012	0.0002	77	1
YG1815-23	322.69	982.2	0.38	0.0469	0.0025	0.0755	0.0038	0.0113	0.0003	73	2
YG1815-24	566.3	1469.47	0.45	0.0487	0.0027	0.0768	0.0037	0.0113	0.0003	73	2
YG1815-25	1135.84	1404.73	0.93	0.0498	0.0023	0.0793	0.0033	0.0114	0.0002	72	1
YG1815-27	926.82	1816.04	0.57	0.0471	0.0021	0.0814	0.0033	0.0121	0.0002	78	2
YG1815-28	780.74	1955.25	0.5	0.0465	0.0021	0.0814	0.0031	0.012	0.0002	77	1
YG1815-29	1586.8	2004.38	0.97	0.047	0.0018	0.0744	0.0027	0.0111	0.0002	71	1
YG1815-30	2077.29	2308.03	1.1	0.0507	0.0019	0.0811	0.0028	0.0113	0.0002	72	1
YG1815-31	1884.5	5573.52	0.45	0.0491	0.0018	0.0866	0.003	0.0127	0.0003	82	2
YG1821-1	972.85	2124.22	0.47	0.0471	0.0013	0.1229	0.0035	0.0187	0.0003	120	2
YG1821-2	2863.57	3107.26	1	0.047	0.0012	0.1233	0.0032	0.0187	0.0002	120	2
YG1821-3	2801.67	2535.26	1.18	0.0477	0.0014	0.1154	0.0035	0.0173	0.0003	111	2
YG1821-4	3247.34	3456.61	1.01	0.049	0.0013	0.1246	0.0032	0.0182	0.0002	116	2

YG1821-5	1310.14	1726	0.81	0.0495	0.0019	0.1257	0.0047	0.0181	0.0003	116	2
YG1821-6	823.41	1756.388	0.51	0.0485	0.0017	0.1239	0.0045	0.0183	0.0003	117	2
YG1821-7	2841.3	3117.48	0.98	0.0479	0.0013	0.1251	0.0034	0.0189	0.0003	121	2
YG1821-8	887.1	1309.61	0.74	0.0498	0.0018	0.1219	0.0042	0.0176	0.0002	112	2
YG1821-9	2480.72	2855.21	0.94	0.0467	0.0012	0.1244	0.0032	0.0192	0.0002	123	2
YG1821-10	759.53	1097.45	0.75	0.0499	0.0021	0.1332	0.0052	0.0189	0.0003	121	2
YG1821-11	1770.32	2107.4	0.91	0.0485	0.0015	0.1246	0.0037	0.0186	0.0003	119	2
YG1821-12	940.9	1325.97	0.75	0.0514	0.0022	0.1309	0.0052	0.0187	0.0003	119	2
YG1821-13	855.83	1323.24	0.71	0.0496	0.0017	0.124	0.0041	0.018	0.0003	115	2
YG1821-14	3469.31	3753.26	0.98	0.0488	0.0013	0.1277	0.0033	0.0189	0.0002	121	2
YG1821-15	5605.03	5164.14	1.19	0.0485	0.0012	0.1266	0.0031	0.0189	0.0003	120	2
YG1821-16	1289.79	2642.69	0.53	0.0512	0.0016	0.1328	0.0039	0.0189	0.0003	120	2
YG1821-17	597.12	1266	0.51	0.0527	0.0021	0.1311	0.005	0.0181	0.0003	115	2
YG1821-18	913.03	1375.23	0.75	0.0496	0.0021	0.1249	0.0047	0.0184	0.0003	117	2
YG1821-19	1114.83	2528.37	0.47	0.0489	0.0015	0.1265	0.0037	0.0188	0.0003	120	2
YG1821-20	2388.36	3253.89	0.8	0.0496	0.0017	0.1255	0.0039	0.018	0.0003	115	2
YG1821-21	628.8	955.32	0.72	0.0473	0.0021	0.1261	0.0047	0.0184	0.0003	117	2
YG1821-22	1046.43	1434.08	0.79	0.0509	0.0022	0.1197	0.0049	0.0173	0.0003	110	2
YG1821-23	1322.62	1933.99	0.73	0.0483	0.0015	0.1181	0.0035	0.0177	0.0002	113	2
YG1821-24	400.96	671.84	0.65	0.0473	0.0025	0.1361	0.0058	0.0187	0.0004	120	2
YG1821-25	2278.65	2544.54	0.95	0.048	0.0014	0.1239	0.0033	0.0187	0.0003	119	2
YG1821-26	3917.48	3718.18	1.04	0.0495	0.0012	0.1412	0.0037	0.0205	0.0003	131	2
YG1821-27	682.51	2547.54	0.3	0.0491	0.0016	0.1307	0.004	0.0192	0.0003	122	2
YG1821-28	186.71	620.97	0.33	0.0457	0.0029	0.1406	0.0066	0.0192	0.0004	122	2
YG1821-29	820.83	1342.29	0.65	0.0496	0.0018	0.1368	0.0052	0.0198	0.0004	126	2
YG1821-30	3950.06	3757.38	1.15	0.0473	0.0014	0.1291	0.0038	0.0197	0.0003	126	2

YG1821-31	1055.72	1418.34	0.83	0.0497	0.0021	0.1195	0.0043	0.0175	0.0003	112	2

Note: Pbr represents radiogenic lead; ages used ^{204}Pb common lead to correct.

Table S3. Zircon (U-Th)/He replicate analyses

Sample	Mass (μg)	238U (ppm)	232Th (ppm)	4He (ncc)	eU (ppm)	Raw age (Ma)	Ft	Corrected Age ± 1σ (Ma)	Mean age ± 1σ (Ma)
YG1701z1	3.28	1094	381	0.100	1184	0.21	0.74	0.28±0.00	
YG1701z2	2.22	1103	254	0.070	1163	0.22	0.71	0.30±0.00	
YG1701z3	4.22	4874	163	0.740	4913	0.31	0.77	0.40±0.00	
YG1701z4	1.93	736	200	0.030	783	0.20	0.71	0.28±0.00	
YG1701									**0.32±0.06**
YG1802-2	3.21	600	282	0.118	666	0.47	0.74	0.63±0.00	
YG1802-3	4.77	327	107	0.087	353	0.44	0.78	0.56±0.00	
YG1802-4	3.97	167	73	0.060	184	0.70	0.76	0.92±0.01	
YG1802									**0.70±0.19**
YG1805-1	3.02	979	1191	1.402	1259	3.03	0.73	4.15±0.01	
YG1805-2	6.14	1404	798	4.883	1591	4.20	0.76	5.49±0.01	
YG1805-3	3.43	902	511	1.320	1022	3.16	0.75	4.23±0.01	
YG1805-4	5.17	1224	377	3.767	1312	4.71	0.76	6.23±0.01	
YG1805-5	5.62	582	465	1.549	692	3.31	0.78	4.27±0.01	
YG1805									**4.87±0.94**
YG1807-1	4.73	1622	948	1.433	1845	1.38	0.76	1.80±0.00	
YG1807-2	3.06	2520	1728	2.808	2926	2.62	0.72	3.63±0.01	
YG1807-3	2.52	2443	1713	1.651	2845	1.92	0.71	2.71±0.00	
YG1807-4	1.61	1144	238	1.128	1200	4.98	0.68	7.31±0.01	
YG1807									**3.86±2.42**
YG1810-1	3.63	4284	4034	5.295	5232	2.31	0.73	3.16±0.01	
YG1810-2	4.37	1323	916	1.873	1539	2.33	0.75	3.11±0.01	
YG1810-3	3.60	3448	1796	4.393	3870	2.65	0.73	3.65±0.01	

YG1810-4	2.95	2886	1670	2.511	3278	2.18	0.72	3.04±0.01	
YG1810-5	3.09	1871	1811	2.322	2296	2.71	0.71	3.79±0.01	
YG1810									**3.35±0.35**
YG1811-1	8.02	3063	994	12.476	3297	4.00	0.79	5.03±0.01	
YG1811-2	5.41	4150	1860	16.646	4587	5.65	0.76	7.48±0.01	
YG1811-3	4.91	1978	782	5.641	2162	4.49	0.76	5.93±0.01	
YG1811-4	4.45	2863	1483	8.439	3211	4.97	0.75	6.65±0.01	
YG1811-5	2.77	5436	2022	7.108	5911	3.67	0.71	5.13±0.01	
YG1811									**6.05±1.04**
YG1812-1	4.55	463	196	1.085	509	3.95	0.77	5.16±0.01	
YG1812-2	12.29	514	155	5.560	550	6.98	0.84	8.34±0.06	
YG1812-3	7.61	1083	275	4.990	1147	4.86	0.79	6.14±0.04	
YG1812-4	16.41	765	181	8.040	807	5.16	0.85	6.11±0.05	
YG1812-5	9.01	433	149	2.730	468	5.49	0.81	6.77±0.01	
YG1812									**6.50±1.17**
YG1814-1	4.27	1255	936	3.400	1475	4.50	0.74	6.10±0.04	
YG1814-2	22.06	641	530	11.040	766	5.43	0.86	6.32±0.06	
YG1814-3	15.80	1670	830	14.660	1865	4.19	0.85	4.93±0.04	
YG1814-4	6.94	1937	692	7.710	2100	4.48	0.80	5.61±0.05	
YG1814-5	3.29	2498	853	3.690	2698	3.53	0.74	4.77±0.01	
YG1814									**5.55±0.69**
YG1815-1	3.53	579	507	0.830	698	2.79	0.74	3.74±0.01	
YG1815-2	3.90	1034	564	1.740	1166	3.21	0.74	4.31±0.01	
YG1815-3	3.37	1363	1366	2.550	1684	3.72	0.72	5.14±0.01	
YG1815-4	5.49	994	552	2.720	1124	3.70	0.75	4.91±0.01	
YG1815-5	4.40	1199	743	3.120	1374	4.32	0.76	5.70±0.01	

YG1815									**4.76±0.76**
YG1818-1	2.62	509	265	1.150	572	6.45	0.73	8.87±0.02	
YG1818-2	4.04	180	185	0.540	223	4.90	0.76	6.47±0.01	
YG1818-3	3.68	10286	1710	31.360	10687	6.80	0.75	9.03±0.04	
YG1818-4	2.19	3903	1833	7.390	4334	6.56	0.71	9.21±0.05	
YG1818-5	2.27	5481	807	9.070	5671	6.03	0.72	8.37±0.07	
YG1818									**8.39±1.12**
YG1820-1	5.53	641	448	5.420	746	10.96	0.76	14.46±0.11	
YG1820-2	8.16	1256	1095	12.120	1513	8.14	0.79	10.28±0.05	
YG1820-3	7.38	328	369	2.620	415	7.04	0.78	9.04±0.06	
YG1820-4	8.07	296	334	2.190	374	5.97	0.80	7.44±0.04	
YG1820-5	6.41	769	783	4.790	953	6.47	0.77	8.37±0.06	
YG1820									**9.92±2.74**
YG1821-1	2.79	2581	910	8.510	2794	9.26	0.73	12.65±0.14	
YG1821-2	3.20	1832	1176	11.230	2108	13.91	0.74	18.93±0.13	
YG1821-3	4.40	1599	891	12.640	1808	13.32	0.75	17.73±0.20	
YG1821-4	2.57	2036	940	7.340	2257	10.65	0.72	14.84±0.03	
YG1821-5	4.70	2415	1263	13.880	2712	9.15	0.75	12.18±0.09	
YG1821									**15.26±3.00**
YG1822-1	3.61	659	421	4.370	758	13.37	0.75	17.90±0.04	
YG1822-2	3.31	519	354	3.060	602	12.82	0.73	17.49±0.04	
YG1822-3	2.74	878	594	4.020	1018	12.04	0.72	16.70±0.10	
YG1822-4	3.13	664	434	5.000	767	17.43	0.73	23.96±0.15	
YG1822-5	4.96	1429	500	14.620	1546	16.13	0.76	21.17±0.14	
YG1822-6	4.82	609	393	4.950	701	12.23	0.76	16.08±0.08	
YG1822									**18.88±3.05**

Table S4. Apatite (U-Th)/He replicate analyses

Sample	Mass (μg)	238U (ppm)	232Th (ppm)	147Sm (ppm)	4He (ncc)	eU (ppm)	Raw age (Ma)	Ft	Corrected Age ± 1σ (Ma)	Mean age ± 1σ (Ma)
YG1701a1	3.03	16	21	402	0.005	21	0.67	1.00	0.67±0.01	
YG1701a2	3.17	62	12	422	0.004	65	0.16	0.83	0.20±0.00	
YG1701a3	2.53	123	39	647	0.005	132	0.12	0.80	0.15±0.00	
YG1701a4	2.12	16	24	444	0.001	22	0.20	0.83	0.23±0.01	
YG1701										**0.31±0.12**
YG1702a1	1.56	29	359	42	0.003	113	0.14	0.62	0.22±0.00	
YG1702a2	1.22	21	215	48	0.001	72	0.11	0.59	0.18±0.01	
YG1702a3	1.68	29	355	57	0.003	113	0.14	0.63	0.23±0.00	
YG1702a4	1.44	28	309	53	0.002	100	0.12	0.61	0.20±0.00	
YG1702										**0.21±0.01**
YG1805a1	13.83	14	56	493	0.054	27	1.16	0.80	1.44±0.09	
YG1805a2	5.90	11	30	276	0.017	18	1.28	0.75	1.70±0.11	
YG1805a3	16.66	32	50	622	0.260	43	2.91	0.84	3.44±0.21	
YG1805										**2.19±1.09**
YG1810a1	10.86	27	11	92	0.138	29	3.55	0.82	4.34±0.27	
YG1810a2	9.54	23	35	191	0.052	32	1.40	0.80	1.76±0.11	
YG1810a3	8.84	39	13	144	0.062	42	1.38	0.81	1.72±0.11	
YG1810a4	10.32	70	17	96	0.075	73	0.82	0.82	1.00±0.06	
YG1810a5	20.94	39	12	97	0.088	42	0.82	0.85	0.97±0.06	
YG1810										**1.96±1.39**
YG1812a1	13.49	25	36	338	0.098	34	1.75	0.82	2.14±0.13	
YG1812a2	12.53	15	26	372	0.031	21	0.92	0.81	1.14±0.07	
YG1812a3	6.27	31	43	453	0.025	41	0.78	0.74	1.06±0.07	

YG1812a4	6.23	27	38	338	0.080	36	2.88	0.76	3.80±0.24	
YG1812a5	17.86	14	20	210	0.047	19	1.14	0.83	1.38±0.09	
YG1812										**1.90±1.14**
YG1820a1	7.24	10	41	62	0.016	19	0.96	0.77	1.24±0.08	
YG1820a2	8.00	10	49	97	0.020	22	0.95	0.77	1.23±0.08	
YG1820a3	8.61	6	36	84	0.062	15	3.97	0.78	5.07±0.31	
YG1820a4	4.82	7	47	66	0.010	18	0.90	0.73	1.23±0.08	
YG1820a5	3.97	9	48	62	0.009	20	0.88	0.70	1.25±0.08	
YG1820										**2.00±1.71**

Table S5. Values of parameters used in the inversion

Figure	*A priori* erosion rate (km/Ma)	Initial geothermal gradient (°C/km)	Spatial correlation length (km)	Time interval (Ma)
Fig. 2 & Fig. S2	2±1	30	10	2
Fig. S3	2±1	30	10	1
Fig. S4	2±1	30	10	4
Fig. S5	2±1	30	20	2
Fig. S6	2±1	20	10	2
Fig. S7	0.5±0.3	30	10	2

Table S6. Radioisotope concentrations and dose rate ($\dot{D}$) value for sample YG1701

Sample	U(ppm)	Th(ppm)	K (%)	Rb(ppm)	Grain size (μm)	$\dot{D}$ (Gy/ka)
YG1701	0.6±0.1	1.4±0.1	1.82±0.01	80±2	150-250	2.8±0.2

Table S7. List of parameters used for the inversion of exhumation rate from the TL data

	TL□ °C□	Growth			Thermal decay			Athermal decay	Natural TL
		$\dot{D}$ (Gy/ka)	D_0 (Gy)	a	E (eV)	$\log_{10}(s)$	b	$\log_{10}(\rho')$	$\bar{n}_{obs}$
YG1701	250-260	2.8±0.2	1143±22	1.07±0.08	1.47	12.82	1.66	-5.23 ±0.02	0.018±0.002
	260-270		1100±21	1.07±0.07	1.50	12.86	1.65	-5.25 ±0.02	0.022±0.002
	270-280		1063±23	1.08±0.08	1.53	12.88	1.65	-5.28 ±0.02	0.026±0.002
	280-290		1026±30	1.08±0.11	1.56	12.89	1.65	-5.30 ±0.02	0.031±0.003
	290-300		996±40	1.08±0.15	1.59	12.87	1.64	-5.34 ±0.03	0.036±0.003
	300-310		965±50	1.07±0.18	1.62	12.83	1.63	-5.37 ±0.03	0.043±0.004
	310-320		939±58	1.04±0.21	1.64	12.75	1.62	-5.40 ±0.04	0.050±0.004

Table S8. Results of ^{10}Be analysis in this study

Sample	Catchment effective elevation (m)	Drainage area (km^2)	Shielding factor	^{10}Be (atoms/g)	^{10}Be error (atoms/g)	Erosion rate (mm/yr)	Erosion rate uncertainty (mm/yr)
YG1801	4584	13356	0.98	8544	3884	4.08	2.37
YG1803	3924	60	0.97	98209	4326	0.28	0.03
YG1813	4396	280	0.98	15966	2203	2.04	0.34
YG1816	4542	76	0.97	31446	2959	1.12	0.15
YG1819	5043	5553	0.99	111467	4676	0.42	0.04
YG1823	5081	507	0.99	422018	10743	0.12	0.01

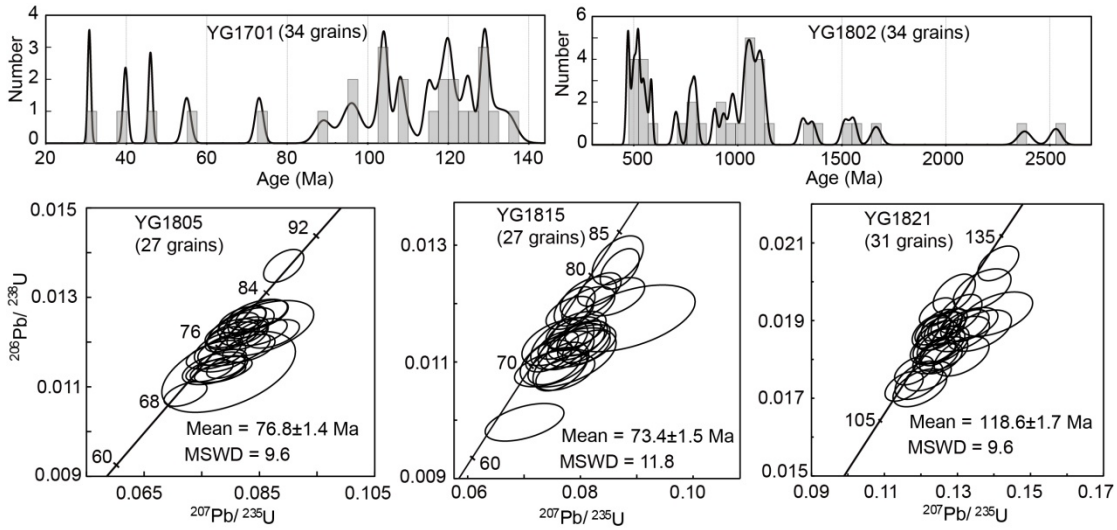

Figure S1. Zircon U-Pb age distribution and concordial plots.

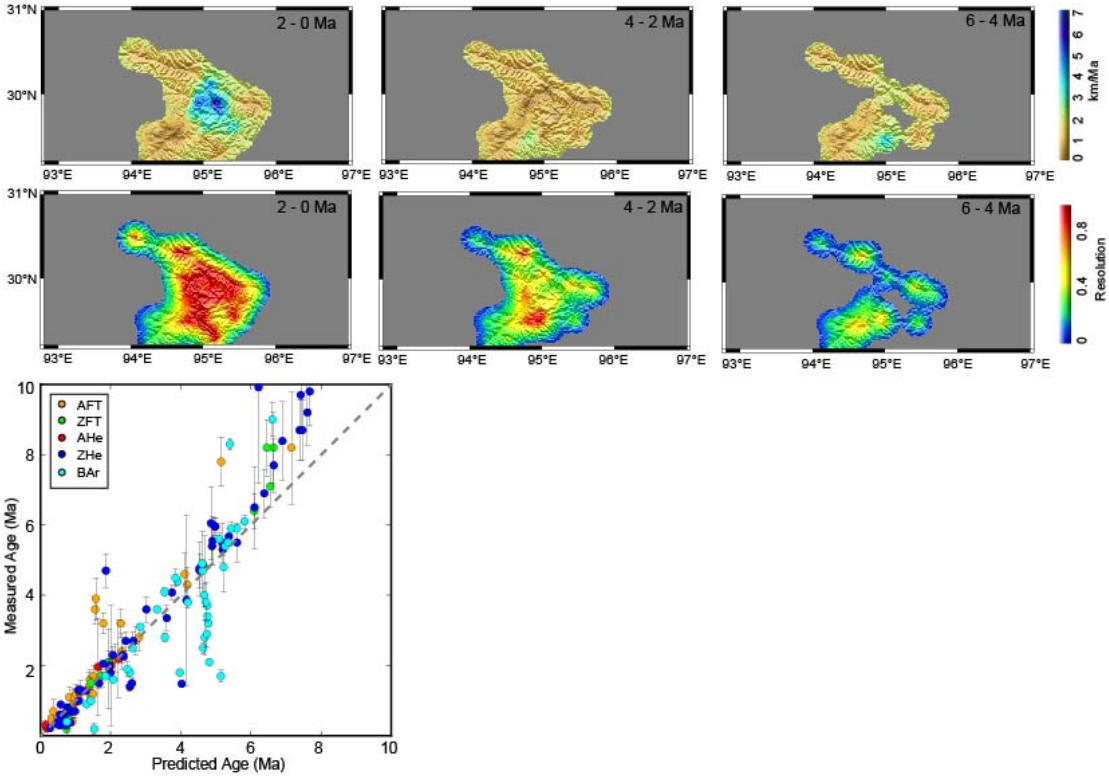

Figure S2. Plots of exhumation rates, resolution and predicted against measured ages using parameters presented in Table S5. The dashed grey line in the bottom left figure is the 1:1 line. AFT-apatite fission-track age; ZFT-zircon fission-track age; AHe-apatite (U-Th)/He age; ZHe-zircon (U-Th)/He age; BAr-biotite $^{40}Ar/^{39}Ar$ age.

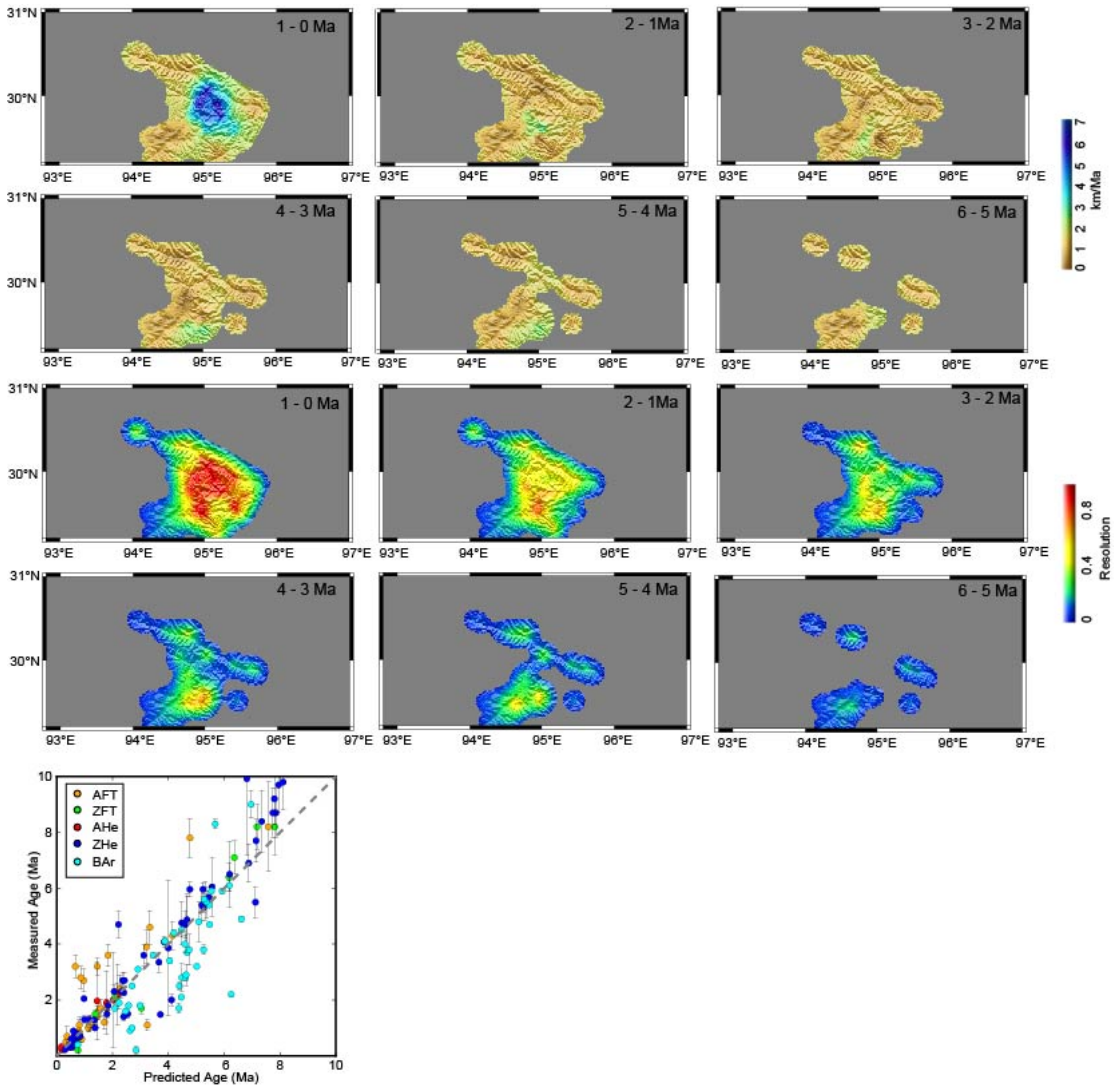

Figure S3. Plots of exhumation rates, resolution and predicted against measured ages using parameters presented in Table S5. The dashed grey line in the bottom left figure is the 1:1 line. AFT-apatite fission-track age; ZFT-zircon fission-track age; AHe-apatite (U-Th)/He age; ZHe-zircon (U-Th)/He age; BAr-biotite $^{40}Ar/^{39}Ar$ age.

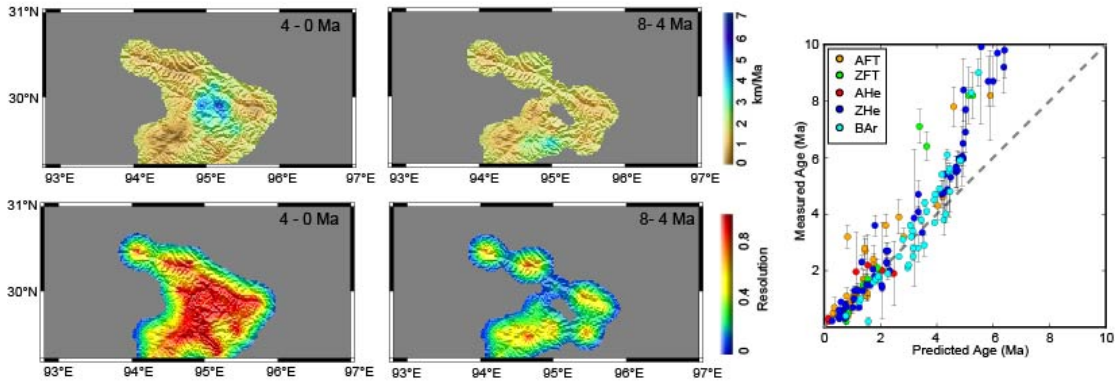

Figure S4. Plots of exhumation rates, resolution and predicted against measured ages using parameters presented in Table S5. The dashed grey line in the bottom left figure is the 1:1 line. AFT-apatite fission-track age; ZFT-zircon fission-track age; AHe-apatite (U-Th)/He age; ZHe-zircon (U-Th)/He age; BAr-biotite $^{40}Ar/^{39}Ar$ age.

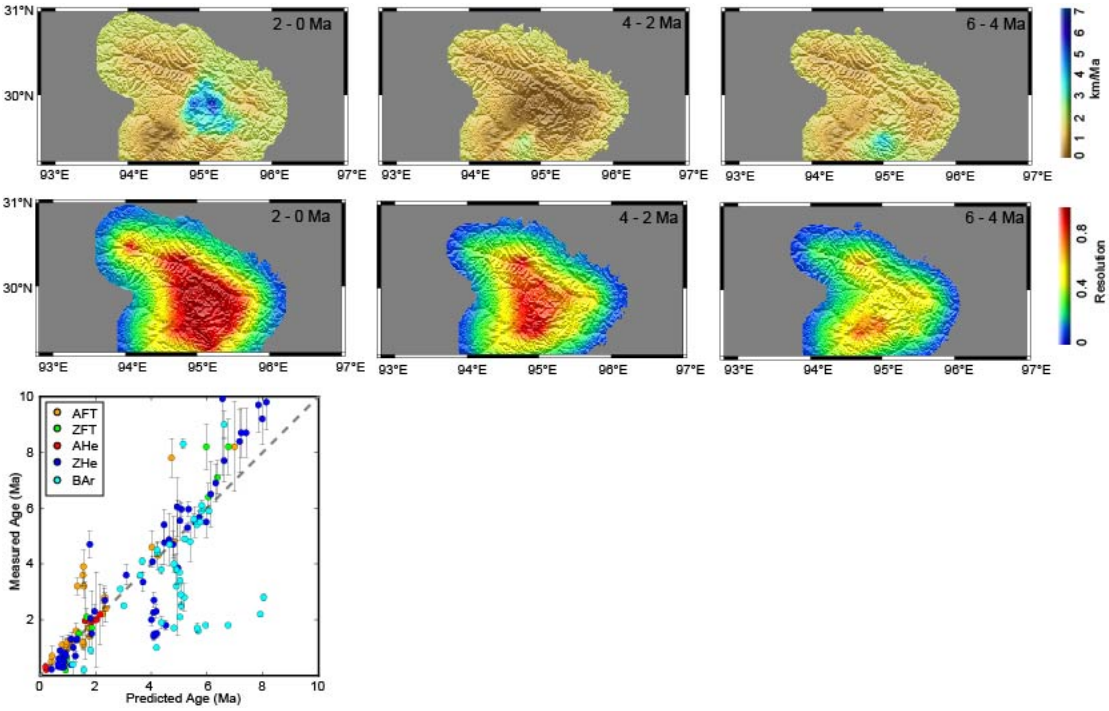

Figure S5. Plots of exhumation rates, resolution and predicted against measured ages using parameters presented in Table S5. The dashed grey line in the bottom left figure is the 1:1 line. AFT-apatite fission-track age; ZFT-zircon fission-track age; AHe-apatite (U-Th)/He age; ZHe-zircon (U-Th)/He age; BAr-biotite $^{40}Ar/^{39}Ar$ age.

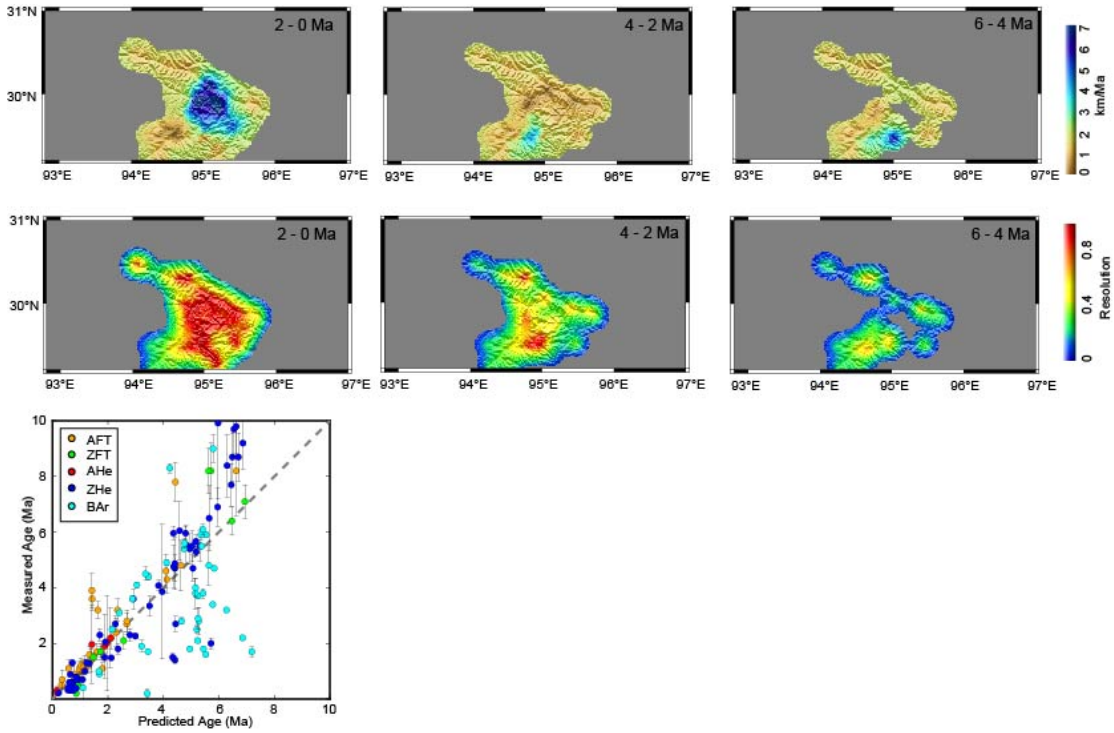

Figure S6. Plots of exhumation rates, resolution and predicted against measured ages using parameters presented in Table S5. The dashed grey line in the bottom left figure is the 1:1 line. AFT-apatite fission-track age; ZFT-zircon fission-track age; AHe-apatite (U-Th)/He age; ZHe-zircon (U-Th)/He age; BAr-biotite $^{40}Ar/^{39}Ar$ age.

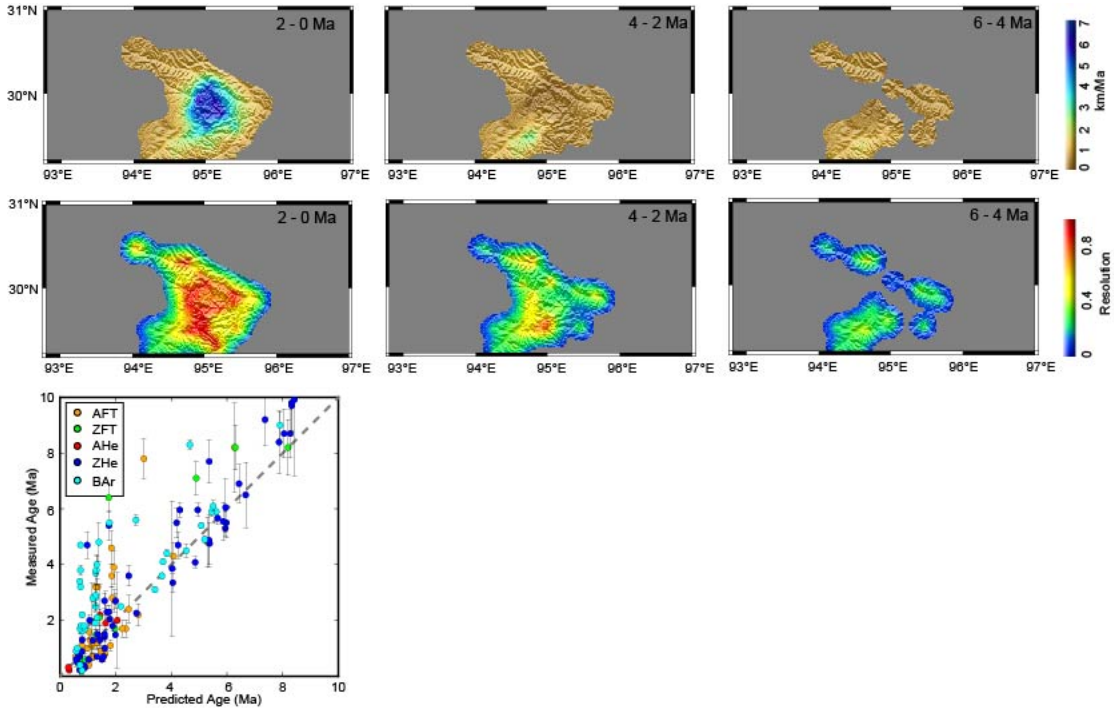

Figure S7. Plots of exhumation rates, resolution and predicted against measured ages using parameters presented in Table S5. The dashed grey line in the bottom left figure is the 1:1 line. AFT-apatite fission-track age; ZFT-zircon fission-track age; AHe-apatite (U-Th)/He age; ZHe-zircon (U-Th)/He age; BAr-biotite $^{40}Ar/^{39}Ar$ age.

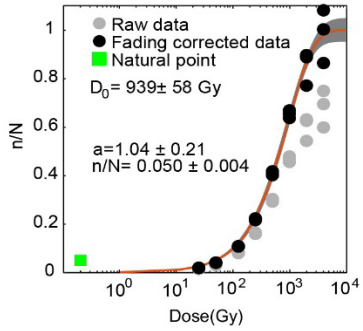

Figure S8. Representative TL growth curve of one signal at 310-320°C for sample YG1701. The gray points are the experimental data. A correction for athermal loss had been made. The un-faded regenerative dose responses (black points) are fitted and the natural TL (nobs), green point, is derived from interpolation onto the fading-corrected dose response curve.

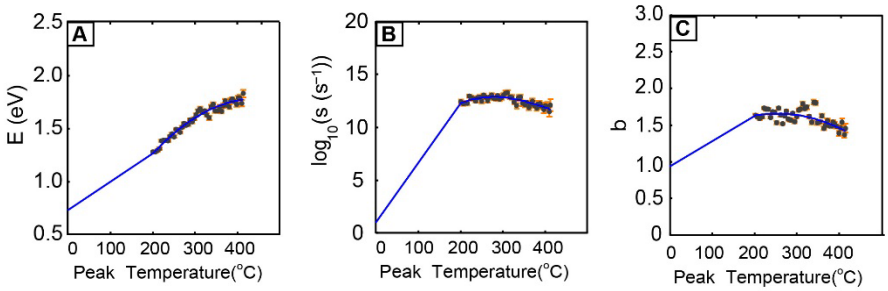

Figure S9. Distribution of kinetic parameters along the glow curve temperature of 200 to 420°C for sample YG1701. A) trap depth (E), B) thermal frequency factor (s) and C) kinetic order of detrapping.

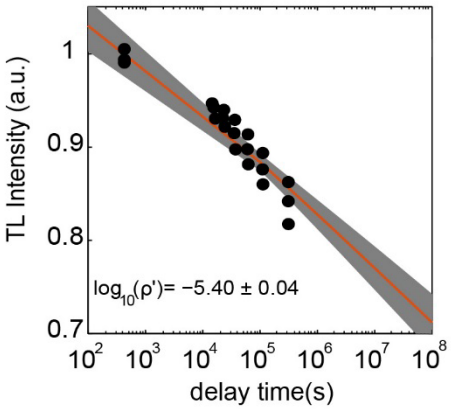

Figure S10. Representative athermal fading of one signal at 310-320° and fitting for sample YG1701.